Investigating the material modelling of a polymeric bioresorbable scaffold via in-silico and in-vitro testing.

Ben Hoddy (b.hoddy@soton.ac.uk)[1], Naveed Ahmed[2], Kadem Al-Lamee[2], Nial Bullett[2], Nick Curzen[3,4], and Neil W. Bressloff[1]

[1]Computational Engineering and Design Research Group, University of Southampton, Southampton, UK
[2]Arterius Ltd, Leeds, UK
[3]Coronary Research Group, Southampton University Hospitals NHS Trust, Southampton, UK
[4]Faculty of Medicine, University of Southampton, Southampton, UK

Abstract

The accurate material modelling of poly-l-lactic acid (PLLA) is vital in conducting finite element analysis of polymeric bioresorbable scaffolds (BRS) to investigate their mechanical performance and seek improved scaffold designs. To date, a large variety of material models have been utilised, ranging from simple elasto-plastic models to high fidelity parallel network models. However, no clear consensus has been reached on the appropriateness of these different models and whether simple, less computationally expensive models can serve as acceptable approximations. Therefore, we present a study which explored the use of different isotropic and anisotropic elasto-plastic models in simulating the balloon expansion and radial crushing of the thin-strut (sub-100 μm) ArterioSorb^{TM} BRS using the Abaqus/Explicit (DS SIMULIA) solution method. Stress-strain data was obtained via tensile tests at two different displacements rates. The use of isotropic and transversely isotropic elastic theories was explored as well as the implementation of stress relaxation in the plastic regime of the material. The scaffold performance was quantified via its post-expansion diameter, percentage recoil and radial strength. The *in-silico* results were validated via comparison with *in-vitro* data of an analogous bench test. Accurately predicting both the post-expansion scaffold shape and radial strength was found to be challenging using the in-built Abaqus models. Therefore, a novel user-defined material model was developed via the VUMAT subroutine which improved functionality by facilitating a variable yield ratio, dependent upon the plastic strain as well as stress relaxation in overly strained elements. This achieved prediction of the specific radial strength within 1.1% of the *in-vitro* results and the scaffold's post expansion diameter within 6.7%. A realistic multi-balloon simulation strategy was also used which confirmed that a mechanism exists in the PLLA which facilitates the extremely low percentage recoil behaviour observed in the ArterioSorb^{TM} BRS. This could not be captured by the aforementioned material property models.

1 Introduction

The withdrawal of the Abbott Vascular bioresorbable vascular scaffold from production led to significant scepticism concerning the efficacy of bioresorbable vascular scaffols (BRS) and their ability to realise clinical benefit. Indeed, it was widely accepted that strut thickness should be markedly decreased for next generation BRS to reduce the risk of late stent thrombosis (LST) without compromise to radial strength (Bink et al. 2019), the feasibility of which remained in question. However, encouraging clinical trial results have rekindled interest in the latest generation of BRS. The Arteriosorb^{TM} BRS, a sub-100 μm strut thickness scaffold, has shown non-inferiority to the XIENCE metallic drug eluting stent (DES) (Katagiri et al. 2019) whilst the Reva Medical Fantom was deemed to have acceptable safety and efficacy after a first-in-man clinical trial (Koltowski et al. 2020). Industry scepticism surrounding BRS has led to many device manufacturers halting the development of polymeric BRS, including Reva Medical, despite the encouraging results for the Fantom scaffold. In addition to the Arteriosorb^{TM}, it appears only a small number of polymeric BRS are currently under development. Whilst more long term data is required, the DESolve by ElixirMedical has also provided encouraging signs, proving its safety and efficacy in early clinical trials (Nef et al. 2018). The MeRes100 by Meril Life, a thin-strut BRS has also demonstrated encouraging results displaying favourable efficacy in treating patients with a de novo coronary artery stenosis in a multi-centre trial (Abizaid et al. 2019).

The efficacy of finite element analysis (FEA) has long since been proven as a method of assessing the mechanical performance of coronary stents and scaffolds (Etave et al. 2001, De Beule et al. 2008, Pant et al. 2012). Naturally, the accuracy of the constitutive material model used in FEA is extremely important. A large variety of material property models have been used to capture the behaviour of poly-l-lactid acid (PLLA, the most common material used to construct the back-bone of BRS). PLLA is a biodegradable aliphatic polyester (Farah et al. 2016). Viscoelasticity, viscoplasticity, anisotropy, strain rate dependance and temperature dependance have all been observed experimentally in PLLA (Bergstroem & Hayman 2016). However, the degree to which it is necessary to model each of these features remains subject to debate. Indeed, it is unclear whether simple material models, used appropriately, provide an acceptable first approximation to model the mechanical performance of BRS without the need for computationally expensive material models.

The material models utilised in FEA of polymeric BRS range from simple elasto-plastic models more commonly applied to metals, such as those implemented by Qiu et al. (2017) and Wang et al. (2017), to high fidelity parallel network models, as used by Debusschere et al. (2015) and Eswaran

et al. (2011) based upon the work of Bergström & Boyce (2001). In the case of Eswaran et al. (2011), the model captured the viscoplasticity, anisotropy and strain rate dependency of PLLA and was calibrated using uniaxial tensile tests of PLLA specimens. Numerical simulations of the deployment of a single ring of a coronary scaffold were then conducted and validated with physical *in-vitro* testing. Pauck & Reddy (2015) were the first to utilise an anisotropic material model in the context of simulating a realistic scaffold deployment. This method used the Hill's yield function to devise different yield stresses for each material direction to conduct a comparison of the mechanical performance of three scaffold platforms via FEA. Wang et al. (2018) conducted extensive *in-silico* testing of a polymeric coronary scaffold utilising an isotropic elasto-plastic Johnson-Cook plasticity model to investigate the effect of environment on scaffold mechanical performance. Bobel et al. (2016) conducted a series of mechanical tests on thin film specimens of PLLA manufactured via the solvent casting method to determine the pre-degradation characteristics of PLLA. Both strain rate and temperature dependency were found to be prevalent along with the time-dependant viscoelasticity phenomenon. Bobel & McHugh (2018) then explored the use of a parallel network (PN) model consisting of hyperelastic, plastic and viscoelastic components. The model was calibrated from the aforementioned uniaxial testing before FEA was conducted utilising the PN material model to assess the effect of strain rate and different deployment techniques on the recoil and stress of a PLLA scaffold. Blair et al. (2019*a*) considered the effect of pre-processing on the anisotropic properties of a PLLA film. The effect of strain rate and temperature on the stress-strain data of uni-axial tensile tests was also explored. Analytical equations to model the Young's modulus and yield strength as a function of temperature and the bi-axial stretch ratio for the two material directions were developed.

Whilst the aforementioned studies contribute significantly to the literature and advance the understanding of the material modelling of PLLA in the context of BRS, there is limited validation of FEA with realistic *in-vitro* deployment and mechanical testing of bioresorbable scaffolds. Also, whilst many material models have been investigated, there is no apparent consensus upon which model provides a suitable approximation of the behaviour of PLLA in the context of FEA. In particular, careful consideration of material anisotropy is lacking, and the benefit of capturing this does not appear to have been explored to date.

Therefore, we present a study that compares isotropic, anisotropic and a new user defined material property model calibrated using test data obtained by Arterius Ltd (Leeds, UK), manufacturer of the Arteriosorb^{TM} BRS. FEA was conducted to mimic the *in-vitro* mechanical testing of scaffolds. The *in-silico* data was compared to the physical bench testing results to ascertain the appropriate-

ness of the respective material models. Firstly, we present the comparison of two simple isotropic elasto-plastic material models and a variety of anisotropic material models that utilise the Hill's yield function. Moreover, these anisotropic models explore the use of stress-strain data obtained from uni-axial tensile tests at different displacement rates. Also, the inclusion of the stress relaxation, or 'failure' data is explored in this simple model as well as considering whether to approximate the material's elasticity as isotropic or transversely isotropic. Based upon these initial findings a new model was implemented via the Abaqus VUMAT subroutine. This utilised the Hill's yield function with several amendments made to increase the model's fidelity whilst retaining simplicity and minimising computational cost. Lastly, a higher fidelity simulation was set up, to explore whether accurate representation of the expansion in the *in-vitro* test procedure leads to better prediction of the final shape and radial strength of the scaffold.

2 Materials and Methods

2.1 Scaffold Geometry

A repeating unit of the geometry configured to represent the Arteriosorb^{TM} BRS is shown in **Fig.1**, which has a ring length of 0.7 mm and a strut width of 0.17 mm increased to 0.22 mm at the crown apex (Bressloff et al. 2017). The scaffold consists of 12 rings that have a thickness in the radial direction of 0.095 mm. The connector length is 0.3 mm whilst its width is 0.15 mm. The 3D geometry of the scaffold is shown in **Fig.2**.

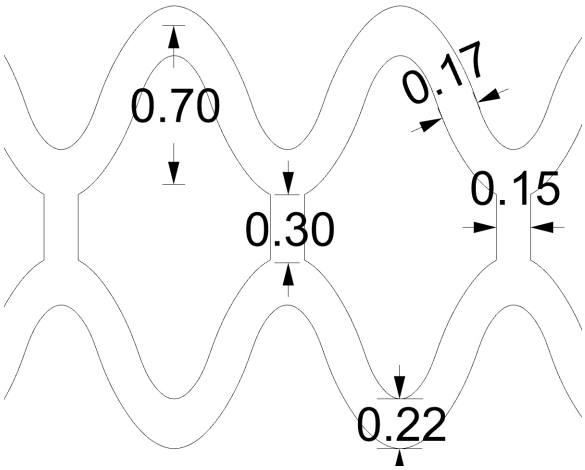

Figure 1: Scaffold geometry for a repeating unit of the central closed ring, based upon the ArterioSorb^{TM} BRS. The width at the crown apex is 0.22 mm, the strut width is 0.17 mm, the ring length is 0.7 mm, the connector length is 0.3 mm and the connector width is 0.15 mm.

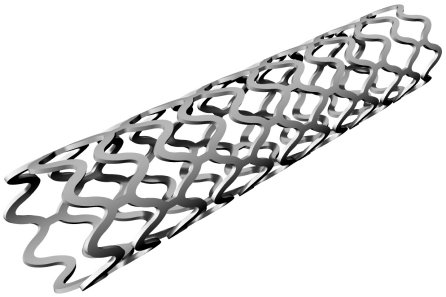

Figure 2: Scaffold geometry based upon the ArterioSorb^{TM} BRS. The scaffold consists of 12 rings, has a length of 12.95 mm, an outer diameter of 2.54 mm and thickness in the radial direction of 0.095 mm.

2.2 Constitutive Material Models

2.2.1 Material Test Data

Uniaxial tensile tests were conducted using a Mecmesin MultiTest 1-I tensometer with U form vice grips on dog-bone specimens. A preload was applied to the samples of approximately 0.1N to remove any slack, such that a region of zero force does not occur in the stress-strain data. Extruded PLLA tubes were processed by solid phase orientation using biaxial die drawing whereby they were heated above the glass transition temperature, then drawn over an expanding mandrel (Al-Lamee et al.

2019). Dog-bone shaped specimens were then laser cut from the die drawn tubes. The stress-strain data obtained was highly realistic and relevant to scaffold design as the PLLA samples were treated identically to the PLLA used to construct the Arteriosorb^{TM} BRS platform to ensure the material properties between dog-bone samples and scaffolds remained constant. The dog-bone specimens had a gauge length of 10 mm and a width of 1.25 mm, as per ISO 20753.

Samples cut from the tube's axial and circumferential directions were tested such that the material anisotropy could be observed. Strain-to-break tests were conducted at four different displacement rates of 1, 5, 10 and 50 mm/min. Two tests were conducted for each direction / displacement rate combination which derived the engineering stress and strain. The averaged data in the two test cases in each scenario was then used to obtain the true stress and strain via the approximations:

$$\sigma_{true} = \sigma_{eng} * (1 + \epsilon_{eng}) \tag{1}$$

$$\epsilon_{true} = ln(1 + \epsilon_{eng}) \tag{2}$$

where the σ_{true} is the true stress, ϵ_{true} is the true strain, σ_{eng} is the engineering stress and ϵ_{eng} is the engineering strain. This was necessary as Abaqus/CAE (DS SIMULIA) requires the true stress and strain values for calibration of the material model, which, for high levels of strain, as considered herein, deviate significantly from the engineering values.

The slowest three displacement rates were deemed clinically relevant given the advice found in the Abbott Vascular BVS product guidelines which recommends a slow rate of expansion due to the relative reduction in stress that this technique induces (Vascular 2017, Bobel et al. 2016). However, Wang et al. (2018) proposed that the efficacy of this technique may be limited in the case of scaffold deployment when submerged in the haemodynamic environment. Simulations were conducted utilising models calibrated to the 1 mm/min and 50 mm/min stress-strain data, respectively. The former considered the most clinically relevant whilst the latter provided a significant point of contrast.

The stress-strain data for uniaxial tensile strain-to-break tests is shown in **Fig.3**. This data was used to calibrate the isotropic, anisotropic and user-defined material models such that they were all based upon the same material data.

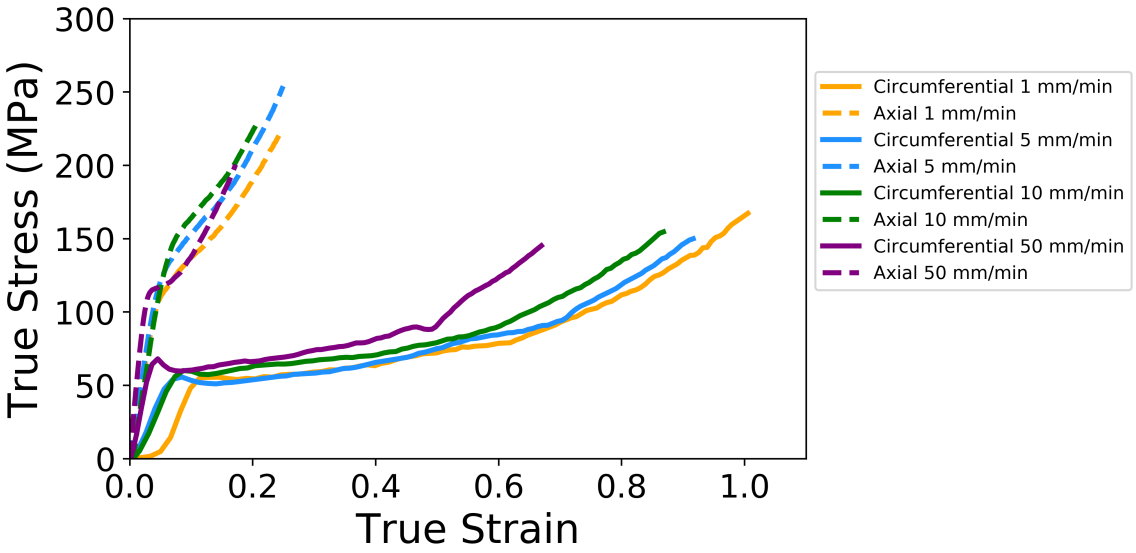

Figure 3: Stress-strain data from uniaxial tensile tests of dog-bone shaped specimens cut from an extruded PLLA tube. Samples from both the axial and circumferential directions were tested at four independent displacement rates. In each case, the sample was strained until failure.

2.2.2 Isotropic Material Model

An elasto-plastic rate independent model which employed the Mises yield function with isotropic hardening was used to model isotropic material behaviour in two different cases utilising the axial and circumferential material properties, respectively. This facilitated a comparison of the two material directions to understand which one was dominant in describing the mechanical behaviour of the scaffold. Only stress-strain data obtained at the displacement rate of 1 mm/min was used for these material models. It was hypothesised that the isotropic models' prediction would be the least accurate of all the models to be evaluated. Therefore, comparison of models calibrated using different stress-strain data was deemed unnecessary.

The Mises yield function reduces the complex 3D stress state of the material and compares this to the yield stress of the material to determine whether it has yielded and thus entered its plastic regime. The underpinning theory of continuum mechanics can be found in Sadd (2018) and Benham et al. (1996). Whilst this model is generally considered more applicable to metals, it is utilised in a number of studies that investigate the mechanical behaviour of polymeric coronary scaffolds (Qiu et al. 2017, Wang et al. 2017). It is also important to consider due to the model's simplicity, ease of implementation and the fact it may provide a reasonable approximation of the macro-behaviour of

this scaffold/PLLA combination.

The material's elastic behaviour is completely described by the bulk modulus, K and the shear modulus, G, defined as:

$$K = \frac{E}{3(1-2\nu)} \tag{3}$$

$$G = \frac{E}{2(1+\nu)} \tag{4}$$

where the Young's modulus, E and Poisson's ratio, ν were input into Abaqus/CAE (DS SIMULIA). Both models used a Poisson's ratio of 0.3.

The Mises stress potential is given by:

$$f(\sigma) = \sqrt{\frac{3}{2} S : S} \tag{5}$$

where S is the deviatoric stress, given by:

$$S = \sigma - \frac{1}{3} trace(\sigma) I \tag{6}$$

where σ is the Cauchy stress tensor and I is the identity matrix.

If the Mises stress exceeds the current yield stress then the material is considered to have yielded. If yielding has not occurred then the stress is obtained via the linear elastic Hooke's law relations (Lautrup 2011). In the case of yielding, the equivalent plastic strain is defined by the approximation:

$$\overline{e}_{pl} = \frac{f(\sigma) - \overline{\sigma}}{3G + H} \tag{7}$$

where $\overline{\sigma}$ is the current yield stress and H is the current hardening of the material.

Whilst an iterative solution technique such as Newton's method may be used to calculate the equivalent plastic strain, for small increments such as those commonly used in the explicit solution technique, Eq.7 is sufficient.

The updated yield stress is then calculated using the equivalent plastic strain. The total stress of the material is then updated using the relation:

$$\sigma = \frac{\overline{\sigma} 2G\hat{e}}{\overline{\sigma} + (3G\overline{e}_{pl})} + \sigma_{hyd} \tag{8}$$

where the term $2G\hat{e}$ gives the elastic deviatoric stress and σ_{hyd} gives the hydrostatic stress (*Abaqus 6.21 Analysis User's Manual* 2018).

The defining properties of each of the isotropic scenarios are shown in **Table 1** and **Table 2**. The Young's modulus, E, defines the slope of the initial portion of the stress-strain curve, preceding the yield stress, σ_y which gives the stress required to cause yielding for a particular strain. In the case of the Abaqus/CAE (DS SIMULIA) isotropic hardening model, the user defines the plastic behaviour by entering the yield stresses as a function of the plastic strain. The hardening is subsequently calculated from the gradient of the stress-strain data as a piecewise linear hardening curve. The initial yield stress at zero plastic strain was calculated using the graphical 0.2% proof method.

Material Direction	**Young's Modulus (Mpa)**
Axial	2985
Circumferential	759

Table 1: Elastic properties for the axial and circumferential data isotropic scenarios.

Axial Direction 1 mm/min		**Circumferential Direction 1 mm/min**		**Circumferential Direction 50 mm/min**	
Plastic Strain ϵ^{pl}	**Yield Stress** σ_y	**Plastic Strain** ϵ^{pl}	**Yield Stress** σ_y	**Plastic Strain** ϵ^{pl}	**Yield Stress** σ_y
0.000	110	0.000	50	0.000	60
0.030	123	0.166	56	0.131	65
0.048	134	0.280	62	0.209	69
0.066	142	0.377	71	0.280	75
0.083	151	0.467	77	0.346	79
0.100	162	0.544	86	0.406	89
0.116	173	0.608	99	0.462	96
0.131	184	0.664	114	0.510	115
0.145	197	0.712	131	0.557	129
0.159	211	0.753	149	0.600	146
0.173	225	0.796	164	0.619	155

Table 2: Plastic properties for the isotropic scenarios utilising stress-strain data obtained at 1 mm/min. The circumferential data obtained at both 1 mm/min and 50 mm/min was also used to define the in-plane plastic behaviour of the PLLA for the anisotropic models.

2.2.3 Anisotropic Material Model

Eight variants of a material model utilising the Hill's yield function (Hill 1948, *Abaqus 6.21 Analysis User's Manual* 2018) were investigated. These explored whether to model the elastic behaviour of the scaffold as isotropic or transversely isotropic and if modelling failure of the material elements via including the stress relaxation data is beneficial. This simply requires the addition of plastic stress-strain data to describe the reduction in stress that occurs as elements become overly strained. In each case, the data obtained at the two different displacement rates was utilised to compare its effect on scaffold mechanical behaviour.

The features of each model are summarised in **Table 3**, comprising the 12 different material model scenarios investigated. Scenarios 3-10 denote the anisotropic Hill's yield function models. The displacement rate at which the stress-strain data used to calibrate the model was obtained is detailed, followed by the elastic and plastic constitutive model theories and lastly whether the stress

relaxation data is employed by the material model.

Test Scenario	**Displacement Rate of Stress-Strain Data (mm/min)**	**Elastic Model**	**Plastic Model**	**Stress Relaxation Data Included**
1 1-Ax-Iso-Mises-N	1 (Axial Direction)	Isotropic	Isotropic (Mises)	No
2 1-Cir-Iso-Mises-N	1 (Circumferential Direction)	Isotropic	Isotropic (Mises)	No
3 1-Cir-Iso-Hill-N	1	Isotropic	Anisotropic (Hill)	No
4 50-Cir-Iso-Hill-N	50	Isotropic	Anisotropic (Hill)	No
5 1-Cir-TrIso-Hill-N	1	Transversely Isotropic	Anisotropic (Hill)	No
6 50-Cir-TrIso-Hill-N	50	Transversely Isotropic	Anisotropic (Hill)	No
7 1-Cir-TrIso-Hill-Y	1	Transversely Isotropic	Anisotropic (Hill)	Yes
8 50-Cir-TrIso-Hill-Y	50	Transversely Isotropic	Anisotropic (Hill)	Yes
9 1-Cir-Iso-Hill-Y	1	Isotropic	Anisotropic (Hill)	Yes
10 50-Cir-Iso-Hill-Y	50	Isotropic	Anisotropic (Hill)	Yes
11 1-Cir-Iso-HB-Y	1	Isotropic	Anisotropic (Hoddy-Bressloff)	Yes
12 1-Cir-Iso-HB-Y*	1	Isotropic	Anisotropic (Hoddy-Bressloff)	Yes

Table 3: Test scenarios and descriptions of their respective material models. Each model is calibrated to stress-strain data which is obtained at one of two different displacement rates and comprises an elastic and plastic model to describe the material behaviour. In the plastic model *Mises* refers to the Mises yield function with isotropic hardening, *Hill* refers to plastic potential theory with the Hill yield function and *Hoddy-Bressloff* refers to the Hoddy-Bressloff model which facilitates a variable plastic potential dependant upon the equivalent plastic strain. *Test scenario 12 (1-Cir-Iso-HB-Y*) used the realistic multi-balloon expansion strategy.

The material's elastic behaviour, when modelled as isotropic is defined by the Young's modulus, E which is calculated as an average of the Young's moduli in the axial and circumferential directions.

Transverse isotropy specifies a single direction in which the material properties vary from an assumed plane of isotropy. This is most appropriate in the case of PLLA as the circumferential and radial directions are assumed to have identical material properties whilst the axial direction deviates from this significantly, as evidenced in **Fig.3**.

E_p gives the Young's modulus in the plane of isotropy, whilst E_t gives the Young's modulus in the transverse direction, in this case, the axial direction of the scaffold. Eq.9 shows the stress-strain relationship for this model whilst Eq.10 and 11 define G_t, the shear modulus in the transverse direction and G_p, the shear modulus in the plane of isotropy in terms of the other parameters (Amadei 1996, *Abaqus 6.21 Analysis User's Manual* 2018). The respective values of ν, the Poisson's ratio, for the different loading directions are extremely difficult to obtain experimentally, particularly for the radial direction. However, Eq.12 shows the relationship between ν_{tp} and ν_{pt}, which, in general are not equal and so assuming ν_{tp} is 0.3, ν_{pt} can be calculated. This is expected to be close to zero, given the increased stiffness in the transverse direction.

$$\begin{Bmatrix} \epsilon_1 \\ \epsilon_2 \\ \epsilon_3 \\ \gamma_{12} \\ \gamma_{13} \\ \gamma_{23} \end{Bmatrix} = \begin{bmatrix} \frac{1}{E_p} & \frac{-\nu_p}{E_p} & \frac{-\nu_{tp}}{E_p} & 0 & 0 & 0 \\ \frac{-\nu_p}{E_p} & \frac{1}{E_p} & \frac{-\nu_{tp}}{E_p} & 0 & 0 & 0 \\ \frac{-\nu_{pt}}{E_p} & \frac{-\nu_{pt}}{E_p} & \frac{1}{E_t} & 0 & 0 & 0 \\ 0 & 0 & 0 & \frac{1}{G_p} & 0 & 0 \\ 0 & 0 & 0 & 0 & \frac{1}{G_t} & 0 \\ 0 & 0 & 0 & 0 & 0 & \frac{1}{G_t} \end{bmatrix} \begin{Bmatrix} \sigma_1 \\ \sigma_2 \\ \sigma_3 \\ \tau_{12} \\ \tau_{13} \\ \tau_{23} \end{Bmatrix} \tag{9}$$

$$\frac{1}{G_t} = \frac{1}{E_p} + \frac{1}{E_t} + 2\frac{\nu_{pt}}{E_t} \tag{10}$$

$$\frac{1}{G_p} = \frac{2(1+\nu_p)}{E_p} \tag{11}$$

$$\frac{\nu_{tp}}{E_t} = \frac{\nu_{pt}}{E_p} \tag{12}$$

Utilising the relations in Eq.10, 11 and 12, the elastic response can be defined using the coefficients E_p, E_t, ν_p, ν_{tp} and ν_{pt} only.

The anisotropic plastic potential material model, in Pauck & Reddy (2015) used the Hill's yield function, an extension of the Mises function, to define the anisotropic yield of the PLLA (Hill 1948, *Abaqus 6.21 Analysis User's Manual* 2018). In Cartesian coordinates this is defined as:

$$f(\sigma) = \sqrt{F(\sigma_y - \sigma_z)^2 + G(\sigma_z - \sigma_x)^2 + H(\sigma_x - \sigma_y)^2 + 2L\tau_{yz}^2 + 2M\tau_{zx}^2 + 2N\tau_{xy}^2} \tag{13}$$

where the constants F to N are given by:

$$F = \frac{\sigma_0^2}{2}\left(\frac{1}{\bar{\sigma}_{22}^2} + \frac{1}{\bar{\sigma}_{33}^2} - \frac{1}{\bar{\sigma}_{11}^2}\right), G = \frac{\sigma_0^2}{2}\left(\frac{1}{\bar{\sigma}_{33}^2} + \frac{1}{\bar{\sigma}_{11}^2} - \frac{1}{\bar{\sigma}_{22}^2}\right), H = \frac{\sigma_0^2}{2}\left(\frac{1}{\bar{\sigma}_{11}^2} + \frac{1}{\bar{\sigma}_{22}^2} - \frac{1}{\bar{\sigma}_{33}^2}\right) \quad (14)$$

$$L = \frac{3}{2}\left(\frac{\tau_0}{\bar{\tau}_{23}}\right)^2, M = \frac{3}{2}\left(\frac{\tau_0}{\bar{\tau}_{13}}\right)^2, N = \frac{3}{2}\left(\frac{\tau_0}{\bar{\tau}_{12}}\right)^2 \quad (15)$$

the ratios $\bar{\sigma}_{ij}^2/\sigma_0^2$ and $\bar{\tau}_{ij}^2/\tau_0^2$ define the ratio of yield stress in the direction ij (where i and j = 1,2,3) to the yield stress in the tabulated stress-strain data used to define the plastic behaviour shown in **Table 2**. A cylindrical coordinate system was used to aid the appropriate application of anisotropic material properties. Direction 1 refers to the radial direction, direction 2 the circumferential direction and direction 3 the axial direction. The stress-strain data for the circumferential direction was entered into Abaqus/CAE (DS SIMULIA) to define the reference plastic behaviour. The ratio:

$$\bar{\sigma}_{33}^2/\sigma_0^2 = 1.72 \quad (16)$$

was used to scale the plastic yield stresses for the axial direction for both displacement rates. The yield stress ratio for the radial and shear directions was assumed to be unity.

The elastic material property parameters that define the isotropic and transversely isotropic models are shown in **Table 4**.

Displacement Rate	**Young's Modulus In-plane**	**Young's Modulus Transverse**	**Poisson's Ratio**	**Poisson's Ratio**	**Poisson's Ratio**	**Shear Modulus In-plane**	**Shear Modulus Transverse**
$\dot{u}$	E_p	E_t	ν	ν_{tp}	ν_{pt}	G_p	G_t
(mm/min)	**(MPa)**	**(MPa)**	**(-)**	**(-)**	**(-)**	**(MPa)**	**(MPa)**
1	759	2985	0.3	0.3	0.076	292	587
50	2035	4577	0.3	0.3	0.133	782	1189

Table 4: Elastic material model parameters for the anisotropic scenarios.

The resultant material property model is shown in **Fig.4** for the two displacement rates. The model shown in **Fig.4** represents the setup in test scenarios 1-Cir-Iso-Hill-N and 50-Cir-TrIso-Hill-N. The model assumes perfect plasticity is exhibited after the last data point of the material's yield stress and plastic strain. Use of isotropic elasticity would result in the elastic portions of the graphs

displaying the same slope for both directions. Use of the stress relaxation data would show a drop in the yield stress from its maximum value to the yield stress value at zero plastic strain before continuing to exhibit perfect plasticity as shown for the circumferential directions for both strain rates via the black dashed lines. The line displaying larger stress values for each data set denotes the axial direction's response whilst the line displaying lower stress values denotes the circumferential direction's response.

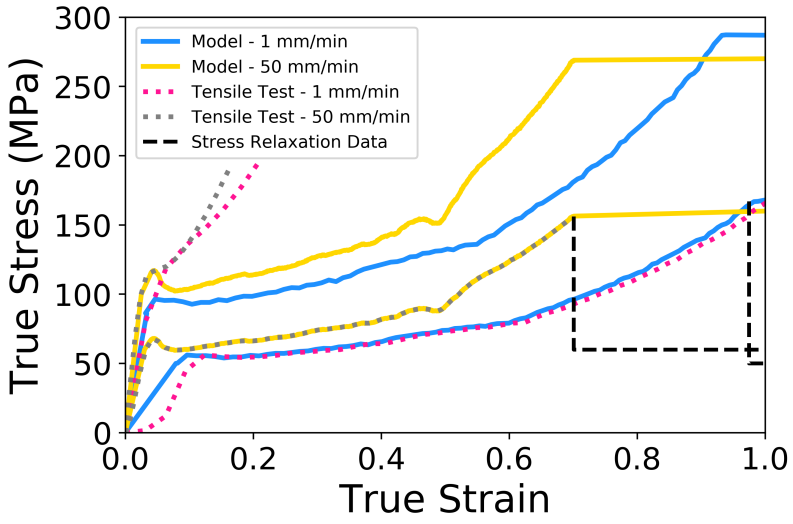

Figure 4: The anisotropic plastic potential material models and tensile test data for the 1 mm/min and 50 mm/min displacement rates. The line displaying lower stress values in each case denotes the response in the circumferential direction whilst the line displaying the larger stress levels in each case gives the axial direction's response. The black dashed line denotes the model's response if the failure data is included, in this case, for the circumferential directions only, to aid observation of the graph.

The plastic hardening in the axial direction of both displacement rates is underestimated in the in-built Abaqus/CAE (DS SIMULIA) anisotropic models. This is a fundamental limitation within the material modelling capabilities of Abaqus/CAE in terms of describing anisotropy in the plastic regime. Only a constant ratio between the yield stresses in the two directions can be used which does not allow the differences in hardening to be captured.

2.2.4 Hoddy-Bressloff Material Model

The inherent limitation of the aforementioned anisotropic material model is evident in **Fig.4** as the hardening in the plastic regime must remain constant between different material directions. Whilst

the Hill's yield function can describe different yield stresses for a given plastic strain in the respective directions, it is unable to capture a difference in the gradients of the stress-strain curves. This is a significant approximation when considering the actual behaviour of PLLA, evidenced in **Fig.3**, where anisotropy is most prolific in the material's plastic behaviour.

To overcome this limitation, the Hoddy-Bressloff material model was developed, based upon the findings of the exploration of the in-built Abaqus/CAE anisotropic material models. The model is based upon the Hill's yield function but defines the yield ratio as a function of the plastic strain rather than a constant value. This facilitates independent rates of change of the yield stress for each material direction, overcoming the limitation of a constant yield potential. This model was implemented using the VUMAT sub-routine in Abaqus/Explicit and provides the same functionality as the aforementioned anisotropic material model with the addition of a variable yield ratio for the axial material direction.

Eq.17 shows the third order polynomial function that defines the ratio of the axial and circumferential yield stresses as a function of plastic equivalent strain. An in-house Python script was developed to optimise the curve fitting to obtain the constants of the polynomial function for input to the material model. This process minimised the least squares residual between the third order polynomial and the ratio of the axial to circumferential yield stresses, obtained in the uni-axial tensile testing.

$$\frac{\sigma_{33}^2}{\sigma_0^2} = 305\bar{e}_{pl}^3 - 53\bar{e}_{pl}^2 + 9\bar{e}_{pl} + 2.26 \tag{17}$$

The elastic behaviour was modelled via isotropic elastic theory using the parameters in Table 5 for the 1 mm/min displacement rate case. The reference plastic data, used to calculate the yield stress and hardening in the circumferential direction, was also approximated via a third order polynomial function, calibrated to the stress-strain data obtained at 1 mm/min, shown in Table 2.

The Hoddy-Bressloff model also facilitates the decrease in hardening and yield stress that occurs when elements exceed their ultimate tensile strain. This allows the elements to effectively fail and so provide no resistance to further deformation by enforcing the plastic hardening and current yield stress to be zero once the ultimate plastic strain for a given element is exceeded. This is in contrast to the in-built Abaqus/CAE anisotropic models that will allow a decrease in hardening and yield stress (although not below the value of the yield stress at zero plastic strain) and thereafter hold the yield stress constant, thus enforcing perfect plasticity upon the material after the ultimate tensile strain is exceeded.

Fig.5 presents the true stress-strain response of the Hoddy-Bressloff model. The drop in stress whereby the plastic strain of the material in the circumferential direction is exceeded is evident.

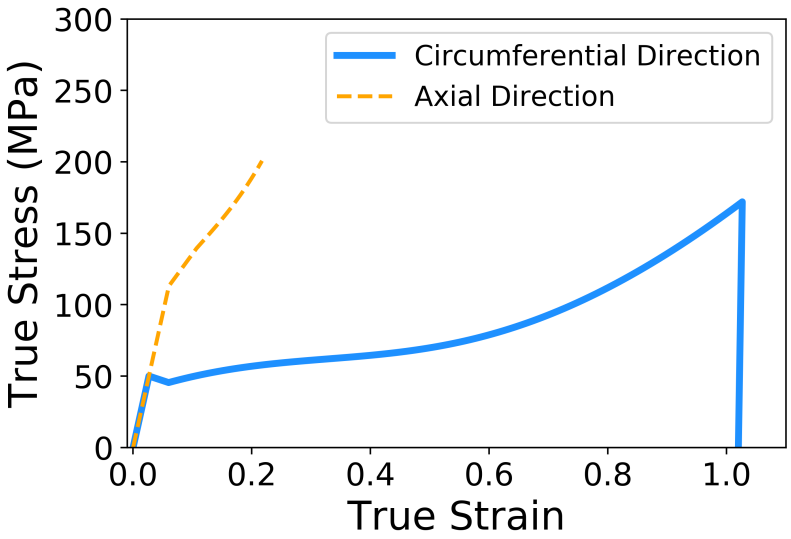

Figure 5: The Hoddy-Bressloff model calibrated using the stress-strain data obtained at 1 mm/min. This utilises a variable yield ratio, dependant upon the plastic strain which facilitates a differential hardening in the plastic regime for the respective material directions. The elastic regime is modelled via simple isotropic relations. The initiation of failure above a true strain of approximately 1.0 is evident whereby the stress relaxes to zero.

2.3 In-vitro Bench Testing

In-vitro testing was conducted by Arterius Ltd (Leeds, UK) to validate the FEA simulations. Firstly, the scaffold was crimped incrementally on to a balloon catheter at 42°C to an outer diameter (OD) of 1.1 mm. The scaffold was then expanded in three stages whilst submerged in a water bath, heated to 37°C. Firstly, a tri-folded balloon of diameter 3.0 mm inflated to 8 and then 16 atm of pressure was used followed by a 3.5 mm diameter balloon inflated to 7.5 atm. This multi-step process is similar to that used in a clinical scenario where post-dilation of the scaffold is commonplace. The OD of each ring in the scaffold was measured throughout the crimping and expansion process at the end of each step. Lastly, the expanded scaffold was radially crushed to an OD of approximately 2 mm using a Blockwise TTR2 radial force testing machine.

2.4 Model Parameters

2.4.1 Simulation Setup

A simulation of the crimping, expansion and specific radial strength tests was conducted to mimic the mechanical *in-vitro* testing of scaffold platforms conducted by Arterius Ltd (Leeds, UK). The simulation consisted of the following steps:

1. Balloon folding. The tapered balloon was wrapped such that it resembled a standard tri-folded balloon.

2. Crimping. The scaffold was crimped from its nominal diameter of 2.54 mm to 1.10 mm via a displacement driven crimping surface. The surface was then removed to allow the scaffold to recoil.

3. Expansion. The scaffold was expanded by inflating the 3.5 mm balloon, pressurised to 7.5 atm. The balloon was then deflated to allow the scaffold to recoil.

4. Crushing. The scaffold was crushed radially via the displacement driven crimping surface to a diameter of 2 mm.

A realistic simulation setup provided two extra 'pre-expansion' steps to the *in-silico* test. This simulation utilised an extra balloon of diameter 3 mm. This smaller balloon was used to pre-dilate the scaffold firstly by being inflated to a pressure of 8 atm and deflated followed by inflation to 16 atm and once again deflated. The simulation then proceeded with step 3 (expansion using the 3.5 mm balloon) as previously described. This method closely followed the technique used by Arterius Ltd (Leeds, UK) in the *in-vitro* testing and was used once for the model described in Table 5, scenario 12. Scenarios 1 - 11 used only a single balloon to expand the scaffold as described in steps 1 - 4. **Fig.6** shows this realistic simulation setup, whilst the standard simulation setup used the 3.5 mm balloon only.

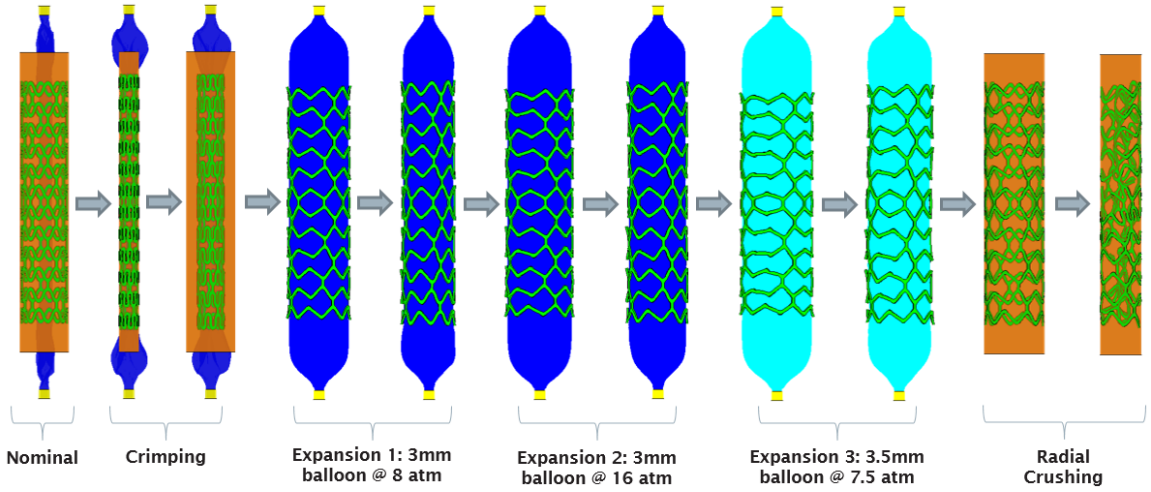

Figure 6: Realistic simulation setup in Abaqus/CAE (DS SIMULIA) to mimic the *in-vitro* testing. The standard simulation setup used the 3.5 mm balloon only to expand the scaffold.

The Abaqus/Explicit solver, as used in many similar studies (De Beule et al. 2008, Grogan et al. 2012, Pant et al. 2012), was chosen due to its ability to handle complex contact interactions. Whilst the solution is time dependant, the inertia forces are not dominant and so the simulation can be approximated as a quasi-static process. Therefore, the kinetic energy of the system should remain low throughout the simulation and should not exceed 5% of the internal energy (*Abaqus 6.21 Analysis User's Manual* 2018). The step lengths and time increment were taken as 0.06 s and 2e-7 s, respectively, based upon previous experience in our group.

The FEA simulations were conducted on the University of Southampton Iridis 4 high performance computing cluster. Each simulation was run on a 2.6 GHz Sandybridge 16-core node and took approximately 6 hours to complete, with the exception of the multi-balloon simulation which took approximately 20 hours to complete.

2.4.2 Scaffold Model

The scaffold was meshed using C3D8R reduced integration elements. These are 8-node 3D stress elements with trilinear shape functions. A mesh refinement study was undertaken where the final diameter and reaction force of the scaffold nodes were found to deviate by less than 4% when refining the mesh from a seed size of 0.04 mm to 0.02 mm, confirming that mesh convergence was achieved. Therefore, a mesh size of 0.04 mm was selected.

2.4.3 Folded Balloon Model

A tapered tri-folded balloon model, similar to that used by De Beule et al. (2008) of length 20 mm was used to expand the scaffold. The isotropic elastic material model was used to describe the behaviour of the balloon where E and ν were taken as 850 MPa and 0.4, respectively. Bilinear 4-node quadrilateral, reduced integration membrane elements were used to mesh the geometry.

2.4.4 Crimp Model

A cylindrical surface of length 20 mm was used to crimp and test the specific radial strength of the scaffold. The crimp was meshed using linear 4-node quadrilateral, reduced integration surface elements.

2.5 Performance

The final diameter and radial strength of a coronary scaffold form the two primary measures of performance. The interventionist seeks to maximise the stented lumen area to restore blood flow whilst the scaffold must have sufficient radial strength to resist the crushing force of a narrowed vessel, which, provides a particular design challenge for thin-strut BRS. The percentage recoil also provides useful insight when considered simultaneously with final diameter. Whilst maximising final diameter may be a priority, minimising percentage recoil could have adverse effects on the stress induced on the vessel wall and the complex process of re-endothelialisation leading to increased levels of restenosis (Onuma et al. 2011, Hoffmann et al. 1996, Pant et al. 2011).

2.5.1 Final Diameter

Final diameter (FD) denotes the outer diameter of a scaffold ring post expansion, once the balloon has deflated and the scaffold has recoiled. An average of the distance between two crowns at the central closed ring and an end ring, respectively is used to calculate the FD and quantify the scaffold's final shape. Ring 1 refers to the central closed ring and ring 6 refers to one of the scaffold end rings, located furthest from the central closed ring.

2.5.2 Recoil

Percentage recoil ($R_{\%}$) is defined as the percentage difference between the maximum diameter of a scaffold ring, at the midway point of the expansion step when the balloon is at maximum inflation

pressure (MD) and the final diameter (FD) at the end of the expansion step, defined as:

$$R_{\%} = (\frac{MD - FD}{MD}) * 100 \tag{18}$$

2.5.3 Radial Strength

Radial strength (RS) is the maximum reaction force of the crimping cylinder, given by the maximum value of the force-displacement curve in the final crushing step. This is defined as:

$$SRS = \sum_{i=1}^{i=3240} F_i \tag{19}$$

where F_i is the reaction force of the i^{th} of the 3240 nodes that constitute the crushing cylinder and l is the length of the scaffold.

3 Results

Results for the 12 test scenarios along with the *in-vitro* bench test are summarised in **Table 5**.

Test Scenario	**Radial Strength (N)**	**Final Diameter Ring 1 (mm)**	**Percentage Recoil Ring 1 (%)**	**Final Diameter Ring 6 (mm)**	**Percentage Recoil Ring 6 (%)**
in-vitro	11.52	3.66	2.92	3.71	2.62
1 1-Ax-Iso-Mises-N	26.42	3.05	17.71	3.14	16.28
2 1-Cir-Iso-Mises-N	6.35	3.14	18.71	3.23	16.71
3 1-Cir-Iso-Hill-N	13.99	3.47	9.88	3.46	10.36
4 50-Cir-Iso-Hill-N	19.30	3.60	6.14	3.57	6.92
5 1-Cir-TrIso-Hill-N	12.82	3.30	14.31	3.29	14.86
6 50-Cir-TrIso-Hill-N	20.33	3.69	4.52	3.53	7.95
7 1-Cir-TrIso-Hill-Y	12.56	3.30	14.29	3.28	15.04
8 50-Cir-TrIso-Hill-Y	19.17	3.60	6.49	3.51	8.47
9 1-Cir-Iso-Hill-Y	14.12	3.47	9.87	3.46	10.36
10 50-Cir-Iso-Hill-Y	15.54	3.69	4.78	3.63	5.96
11 1-Cir-Iso-HB-Y	11.00	3.51	9.65	3.46	11.07
12 1-Cir-Iso-HB-Y*	11.40	3.48	10.44	3.46	10.82

Table 5: Radial strength, final diameter and recoil obtained for the 12 different testing scenarios along with the *in-vitro* bench test results.

Fig.7 shows the plastic equivalent strain developed in the vicinity of the crown apex at the scaffold end rings using **(a)**, material model 1-Ax-Iso-Mises-N and **(b)**, material model 1-Cir-Iso-Mises-N. **Fig.7(a)** shows a much larger magnitude of plastic equivalent strain at the inside of the crown whilst the outside edge of **Fig.7(b)** at the crown appears jagged. This behaviour does not appear to be reflected in *vitro*. There is also very little development of plastic equivalent strain at the outside of the crown in **Fig.7(b)**.

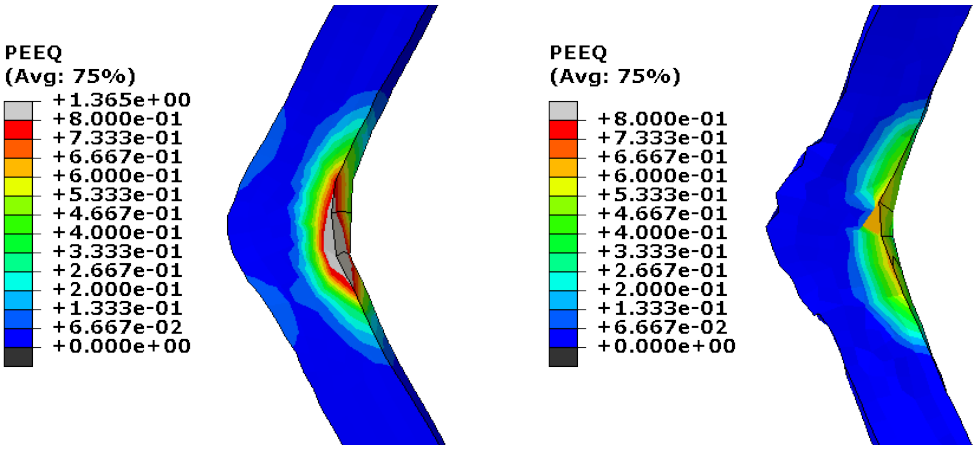

(a) (b)

Figure 7: Plastic equivalent strain distributions for the simulations using isotropic material models that utilise **(a)**, stress-strain data from the axial direction (model 1-Ax-Iso-Mises-N) and **(b)**, stress-strain data from the circumferential direction (model 1-Cir-Iso-Mises-N).

Fig.8 shows a comparison of the plastic equivalent strain developed in the two end rings of scaffolds using models 1-Cir-TrIso-Hill-Y, 50-Cir-TrIso-Hill-Y, 1-Cir-Iso-Hill-Y and 50-Cir-Iso-Hill-Y. Each of these models uses the failure stress-strain data to induce stress relaxation in the elements once the ultimate tensile strain is exceeded. Of particular note is model 50-Cir-TrIso-Hill-Y, shown in **Fig.8(b)**, which displays extremely large levels of $PEEQ$ at the inside of the crowns that would not manifest in the scaffold in *vitro*. Models 1-Cir-TrIso-Hill-Y, **Fig.8(a)**, 50-Cir-Iso-Hill-Y, **Fig.8(b)** and 1-Cir-Iso-Hill-Y, **Fig.8(c)** appear to offer a comparatively more realistic picture of $PEEQ$ distribution in the scaffold struts.

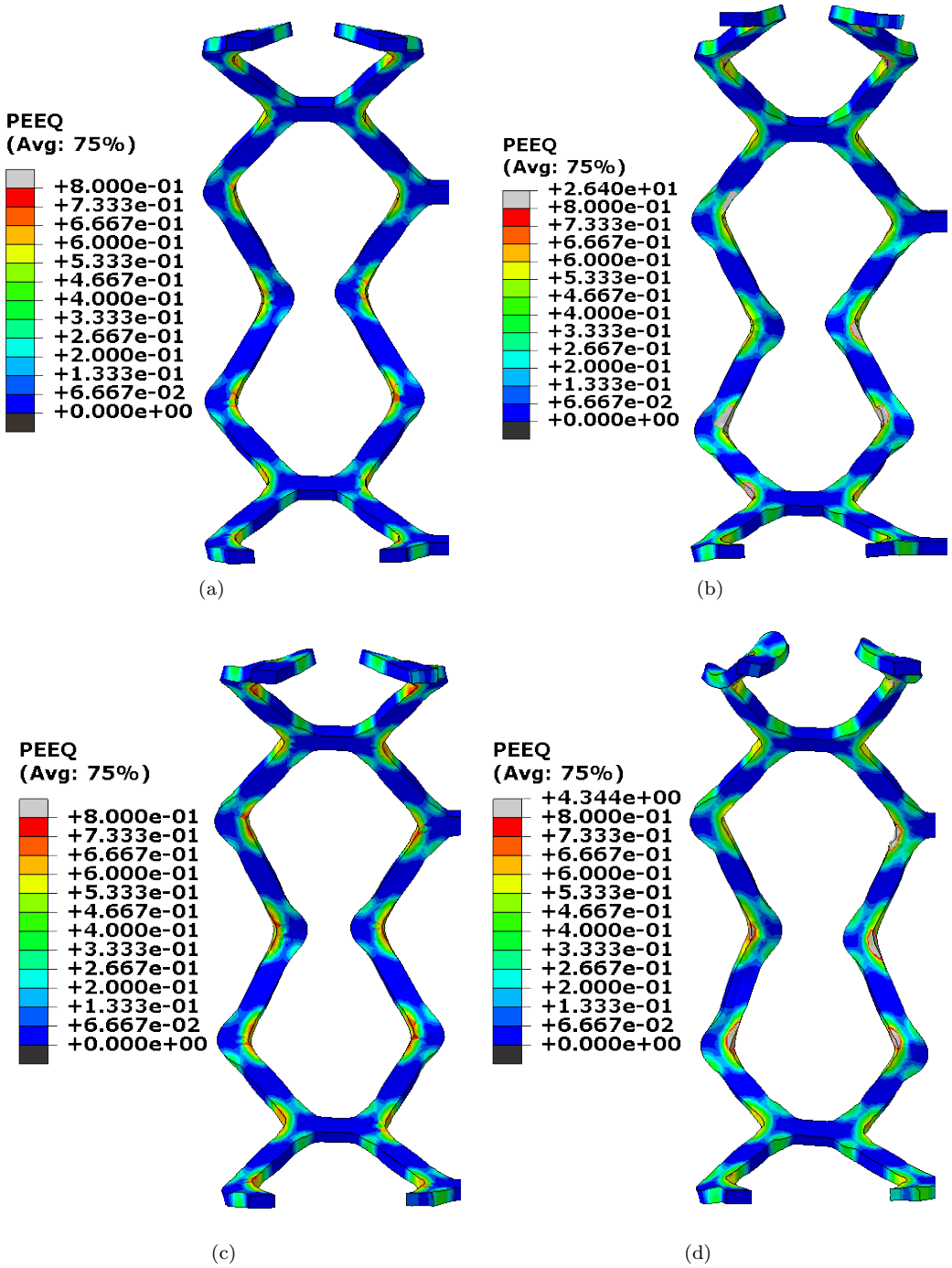

Figure 8: A comparison of the plastic equivalent strain in the end rings of the scaffolds from **(a)**, model 1-Cir-TrIso-Hill-Y **(b)**, model 50-Cir-TrIso-Hill-Y **(c)**, model 1-Cir-Iso-Hill-Y and **(d)**, model 50-Cir-Iso-Hill-Y. The plots are displayed when the scaffold reaches its maximum diameter when the balloon is at maximum inflation pressure.

The plastic equivalent strain in the scaffold struts post recoil for model 50-Cir-Iso-Hill-Y, test scenario 10, is presented in **Fig.9**. The plastic strain distribution appears generally representative of reality with significant levels of $PEEQ$ developed either side of the crown apex on its outer radius. However, very large maximum values of plastic strain, approximately 6 times greater than the ultimate tensile strain observed in the tensile tests of PLLA conducted at 50 mm/min, develop at the inside of the crowns which would not manifest to such a high magnitude in *vitro*.

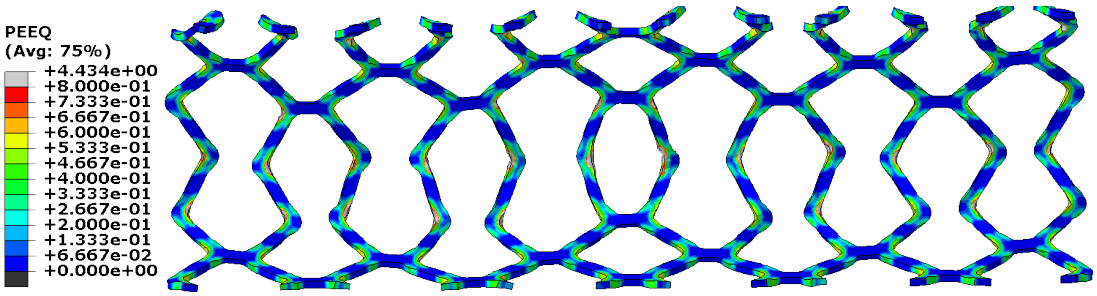

Figure 9: The equivalent plastic strain distribution for the post-expansion recoiled scaffold for model 50-Cir-Iso-Hill-Y, test scenario 10.

Fig.10 shows the force displacement curves for the *in-vitro* test and model 1-Cir-TrIso-Hill-Y, test scenario 7. The anisotropic model predicts the RS well throughout the crushing process with an over-prediction of the maximum force of 9%.

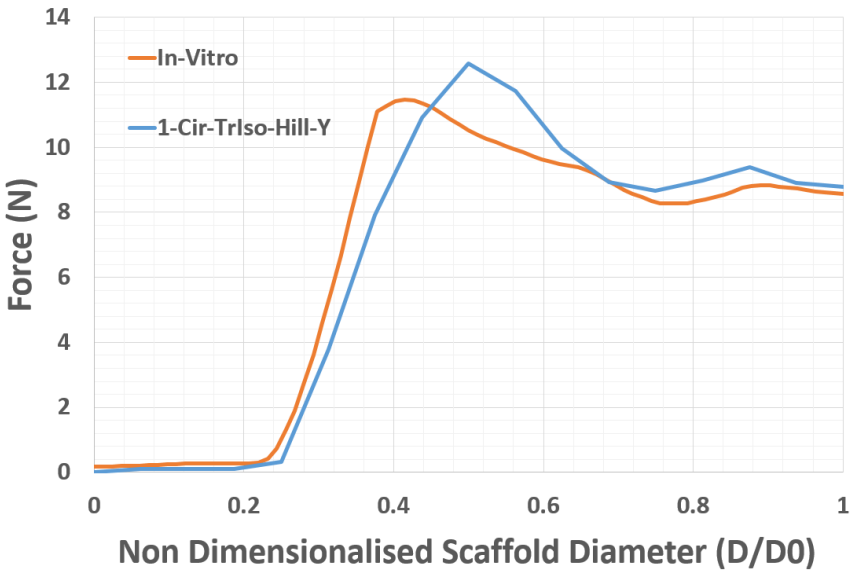

Figure 10: The force-displacement curves from the radial crushing test for the *in-vitro* test and model 1-Cir-TrIso-Hill-Y, test scenario 7, the anisotropic plastic model utilising elastic transverse isotropy and the failure stress-strain data, obtained at a displacement rate of 1 mm/min.

The plastic equivalent strain distribution for the model 1-Cir-Iso-HB-Y, test scenario 11, is shown in **Fig.11**. The maximum plastic strains developed at the inside of the crowns appear to greatly exceed ultimate tensile strain of the PLLA. This is caused when the relaxation of stress occurs due to the ultimate tensile strain being exceeded in the Hoddy-Bressloff model. Elsewhere in the scaffold struts the plastic strain appears more closely confined to the vicinity of the crown apex compared with the in-built Abaqus/CAE anisotropic models.

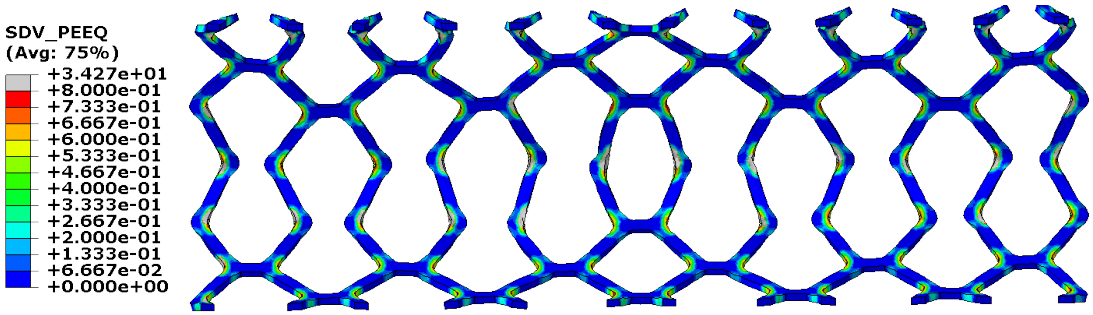

Figure 11: The distribution of plastic equivalent strain in the struts of the ArterioSorb^{TM} once the scaffold has recoiled post expansion for model 1-Cir-Iso-HB-Y.

Fig.12 shows the force-displacement curves for the *in-vitro* test, model 1-Cir-Iso-HB-Y (test

scenario 11) and model 1-Cir-Iso-HB-Y* (test scenario 12). The simulations utilise the same Hoddy-Bressloff model but different deployment strategies. Both cases appear to predict the force required to crush the scaffold until the maximum force after which the scaffold is deemed to have failed. At this point the crushing force prediction deviates significantly from the *in-vitro* test.

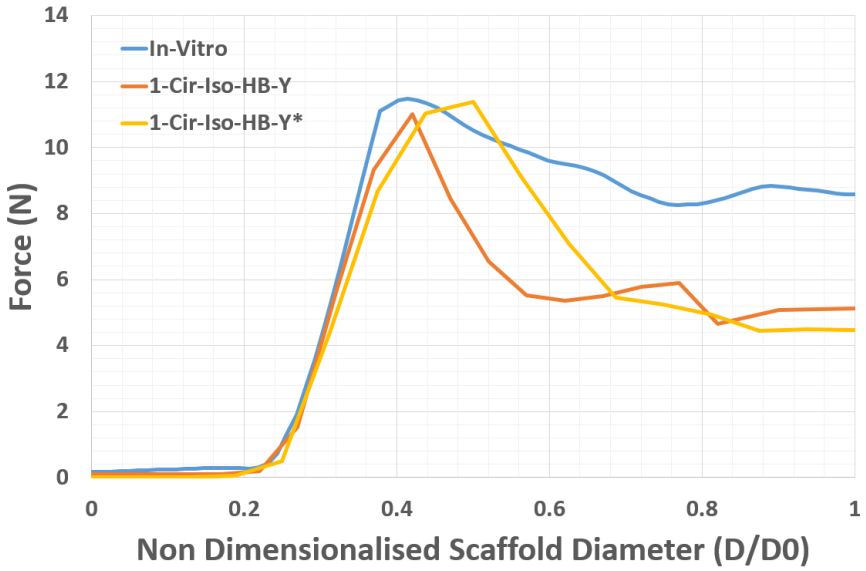

Figure 12: The force-displacement plots from the radial crushing test for the *in-vitro* test as well as models 1-Cir-Iso-HB-Y and 1-Cir-Iso-HB-Y*, both of which use the Hoddy-Bressloff model encompassing linear isotropy, the stress-strain failure data and calibration to the plastic stress-strain data obtained at a displacement rate of 1 mm/min.

4 Discussion

4.1 Tensile Testing of Material Samples

The highly anisotropic properties of PLLA are evident in **Fig.3**. Indeed, the axial direction has a significantly higher stiffness and yield point in comparison to the circumferential direction. However, the ultimate tensile strain is much lower in the case of the axial direction. Interestingly, this is in contrast to the data obtained by Eswaran et al. (2011) and Blair et al. (2019*b*). The crystallinity of the PLLA blend provided by Arterius Ltd was such that the polymer chains were orientated in the axial direction. High strength and low ductility are associated with properties aligned with the polymer chains and so these trends in material anisotropy, presented in **Fig.3**, are expected (Bergstroem & Hayman 2016).

In the circumferential direction, the failure strain is inversely proportional to the displacement rate whilst the yield stress increases, albeit marginally, with an increase in displacement rate. The Young's modulus appears to strongly correlate with displacement rate, ranging from approximately 800 MPa at 1 mm/min to almost 3000 MPa at 50 mm/min in the circumferential direction. In the 1 mm/min case for the circumferential direction, the initial elastic portion of the graph exhibits non-linear elasticity, evidenced by the large change in gradient at low levels of strain.

In the case of the axial direction, the yield point is proportional to the displacement rate. However, the largest displacement rate of 50 mm/min appears to subvert this trend and showed a similar yield point to the 1 mm/min case of 110 MPa. The Young's modulus also increases for the axial direction from 3000 MPa at 1 mm/min to 4500 MPa at 50 mm/min.

From this data it is evident that the anisotropic effects of PLLA are significant whilst the effects of strain rate are generally more subtle. However, the stress-strain response in the circumferential direction showed a significant range of variation in the Young's modulus and ultimate tensile strain between the 1 mm/min and 50 mm/min cases. Considering the findings of Wang et al. (2018), it is possible that the effects of strain rate are even more subtle when the scaffold is deployed inside a vessel at an elevated temperature, meaning that modelling this effect could be unnecessary. Moreover, it should be remembered that the scaffold struts undergo bending about the crown apex as they are expanded, rather than uni-axial tension. This could also lower the stress magnitude in *vitro*, particularly when considering that the ArterioSorb BRS has been observed to withstand significant over-expansion without displaying evidence of strut fracture, as shown in **Fig.13**. It should also be noted that a displacement rate as high as 50 mm/min is unlikely to be encountered in clinical scenarios but provides a significant contrast to the clinically relevant displacement rates.

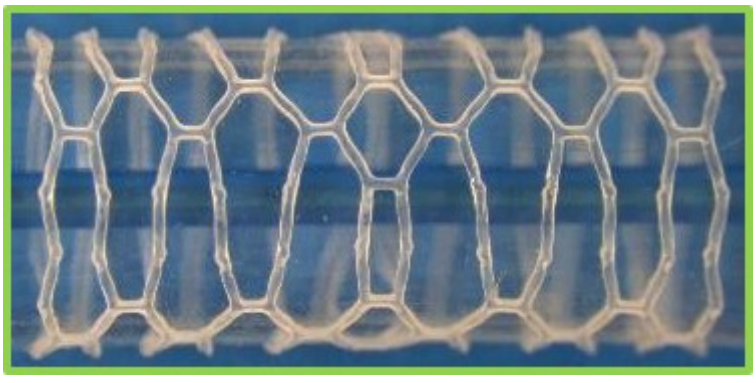

Figure 13: The ArterioSorb^{TM} BRS overexpanded to an outer diameter of 4.4 mm. Straightening of the struts has occured without evidence of strut fracture.

4.2 Isotropic Plastic Material Models

Observation of the isotropic plastic material models' results shows their inferiority compared to anisotropic models. Utilising the axial stress-strain data only (model 1-Ax-Iso-Mises-N) significantly overestimates the RS of the scaffold compared to the *in-vitro* bench test, whilst the circumferential data (model 1-Cir-Iso-Mises-N) underestimates this metric. In both cases the isotropic model provides a poor estimate of the final scaffold shape, predicting a $R_{\%}$ of approximately 18% and FD of approximately 3.1 mm at the central ring compared to 2.92% and 3.66 mm, respectively for the *in-vitro* test. Utilising data obtained at a higher displacement rate would likely further degrade the isotropic axial model and provide minimal improvement to the isotropic circumferential model's prediction, given that this would result in a Young's modulus similar to that used in model 1-Ax-Iso-Mises-N, test scenario 1.

The PEEQ distribution is an important factor in determining the mechanical performance of BRS. **Fig.7** shows the PEEQ distributions at a single crown of the central closed ring when the balloon is at maximum inflation pressure. A high level of PEEQ at the inside of the crown is evident in **Fig.7(a)**. However, the plastic strain on the outside of the crown is extremely low, yet the *in-vitro* data suggests a significant amount of PEEQ develops either side of the crown apex on the outside of the crown. This is evident in **Fig.14** where the outside edge of the crown apex becomes more pronounced due to the adjacent areas of plastic strain as the scaffold opens in expansion. This could be described as 'pinching' of the crown apex. Therefore, it is unlikely that **Fig.7(a)** provides a realistic picture of the strain distribution in the scaffold. **Fig.7(b)** highlights some significant deformation around the outer edge of the scaffold whereby it appears jagged which seems non-physical, perhaps due to the low material stiffness inherent to the circumferential data. There is also no development of PEEQ on the outside of the crown in **Fig.7(b)** and very low levels of PEEQ on the inside of the crown. Therefore, it is clear that isotropic material models provide limited insight into scaffold mechanical behaviour.

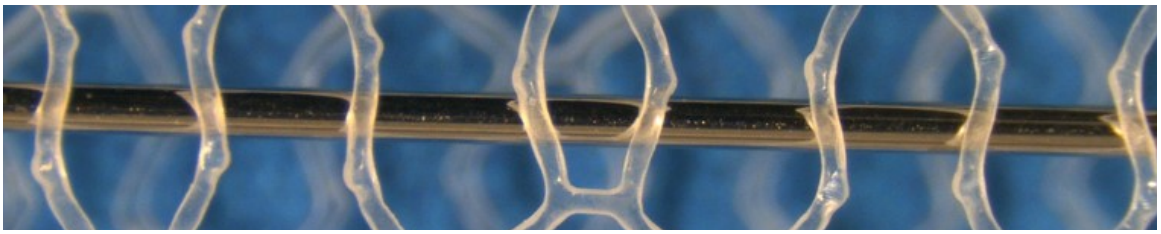

Figure 14: A section of the recoiled ArterioSorb^{TM} BRS. Significant levels of plastic strain have been developed either side of the open-cell crown apexes at their outer edges resulting in 'pinching' of the crown.

4.3 Anisotropic Plastic Material Models

4.3.1 Comparison of Displacement Rate of Underlying Stress-Strain Data

Use of the anisotropic material models provided a clear step change in the predicted mechanical behaviour of the scaffold. Model 1-Cir-Iso-Hill-N significantly improved upon predicting the RS and FD compared to the isotropic material models, resulting in percentage errors of 21% and 6.7%, respectively from the *in-vitro* data. Model 50-Cir-Iso-Hill-N greatly improved upon the FD and $R_{\%}$ prediction, whereby the FD of the scaffold end ring was predicted to within 4% of the *in-vitro* value, compared to the isotropic models yet over estimated the RS, by 40%, due to its high Young's modulus. Models 1-Cir-Iso-Hill-N and 50-Cir-Iso-Hill-N represent the trade-off between prediction of the scaffold shape and radial strength, the former better described in each case by utilising the 50 mm/min stress-strain data to enforce a lower level of recoil while the latter preferring the use of the slower displacement rate data.

4.3.2 Comparison of Elasticity Models

In considering the modelling of the material's elastic regime, utilising an isotropic approximation in the case of the slower displacement rate greatly improved prediction of the scaffold shape (comparing models 1-Cir-Iso-Hill-N and 1-Cir-TrIso-Hill-N) whilst there is no significant difference in the case of the 50 mm/min data (comparing models 50-Cir-Iso-Hill-N and 50-Cir-TrIso-Hill-N). Model 50-Cir-Iso-Hill-N provided percentage errors of 1.64% and 3.77% for prediction of the FD of rings 1 and 6, respectively when compared with the *in-vitro* scenario. However, model 1-Cir-TrIso-Hill-N provided a marked improvement upon the prediction of RS when compared to model 1-Cir-Iso-Hill-N, although at the expense of predicting the scaffold's final shape. Once again, the trade-off between predicting the scaffold shape and RS is highlighted, in this case due to the modelling of the elastic

regime of PLLA.

4.3.3 Use of Failure Stress-Strain Data

Inclusion of the failure data allied with the transversely isotropic elastic model, as per models 1-Cir-TrIso-Hill-Y and 50-Cir-TrIso-Hill-Y, did not significantly alter prediction of the scaffold shape compared to models 1-Cir-TrIso-Hill-N and 50-Cir-TrIso-Hill-N. However, a small improvement in RS prediction was achieved in both cases, due to the relaxation in stress that occurs as elements begin to exceed the ultimate tensile strain. Interestingly, observation of **Fig.8** suggests that only a very small number of elements exceeded the ultimate tensile strain in model 1-Cir-TrIso-Hill-Y, shown in **Fig.8(a)**. However, in model 50-Cir-TrIso-Hill-Y, shown in **Fig.8(b)**, there were elements that exceeded the ultimate tensile strain (remembering that in this case the ultimate tensile strain is lower, approximately 0.65) yet there were only modest changes to prediction of the scaffold's final shape and RS. Further, it is also evident in **Fig.8(b)** that the highly strained areas are generally not joined to a connector. This same trend is evident in a comparison of model 1-Cir-Iso-Hill-Y, **Fig.8(c)** and model 50-Cir-Iso-Hill-Y, **Fig.8(d)**. Therefore, it is possible the mechanical performance of the scaffold is dominated by the geometry of the crowns attached to connectors as, despite the highly strained elements, the scaffold maintains good mechanical performance in the case of models 50-Cir-TrIso-Hill-Y and 50-Cir-Iso-Hill-Y. Comparing models 1-Cir-TrIso-Hill-Y and 1-Cir-Iso-Hill-Y as well as 50-Cir-TrIso-Hill-Y and 50-Cir-Iso-Hill-Y it can be observed that utilising the isotropic elastic approximation led to greater development of plastic strain in both cases which resulted in improved final diameter predictions.

Returning to the distribution of plastic equivalent strain at the outside of the crown, **Fig.8** shows a much more realistic picture compared to **Fig.7**. Significant development of plastic strain either side of the crown apex is evident in **Fig.8** in all test scenarios which results in 'pinching' of the crown observed in the physical bench tests, as per **Fig.13**.

4.3.4 Summary of Anisotropic Plastic Models

Modelling the elastic behaviour of the scaffold using linear isotropy and including the failure data in the material model, as per models 1-Cir-Iso-Hill-Y and 50-Cir-Iso-Hill-Y, yielded a significant improvement in prediction of the final scaffold shape, compared to models 1-Cir-TrIso-Hill-Y and 50-Cir-TrIso-Hill-Y, respectively. Scenario 50-Cir-Iso-Hill-Y also provided an improvement in the prediction of RS as this reduces from 19.17 N in model 50-Cir-TrIso-Hill-Y to 15.54 N. Model 1-Cir-

Iso-Hill-Y achieved a good estimation of scaffold final diameter with percentage errors of 5.19% and 7.89% for rings 1 and 6, respectively. This is extremely good considering the low Young's modulus of just 1872 MPa utilised in that model. However, the prediction of *RS* in the case of model 1-Cir-Iso-Hill-Y, yielded a percentage error of 22.47%, compared to the *in-vitro* test. Utilising an average of the Young's moduli for the axial and circumferential directions to describe the material stiffness, as performed in the implementation of the isotropic elastic models, resulted in an effective increase in stiffness in the circumferential direction. As the circumferential direction is the primary loading direction in expansion, the *RS* was overestimated, evidenced in models 1-Cir-Iso-Hill-Y and 1-Cir-TrIso-Hill-Y when compared to the *in-vitro* test.

After exploration of the models utilising the anisotropic Hill's yield function, considering isotropic and transversely isotropic elastic models, failure stress-strain data and displacement rate of the underlying stress-strain data, it is clear that none of these models can simultaneously capture both the final scaffold shape and specific radial strength for the ArterioSorb^{TM} BRS. Use of the Hill's yield function in combination with elastic isotropy and the failure data (as per model 50-Cir-Iso-Hill-Y) gave the best prediction of final diameter with percentage errors, compared to the *in-vitro* data, of 0.82% and 2.16% for rings 1 and 6, respectively. However, the percentage error for *RS* prediction for this scenario was 34% which represents a significant overestimation. The recoiled scaffold for model 50-Cir-Iso-Hill-Y is presented in **Fig.9**. The maximum plastic strains reach approximately 4.4 at the inside of some crowns, in particular those not attached to a connector. It is noticeable that even after recoil the scaffold struts remain relatively straight, particularly at the central closed ring due to the significant development of plastic strain at this location. Strains of this magnitude would not develop in *vitro* but lead to redistribution of the strain in the scaffold struts or result in failure of the scaffold struts due to ductile fracture. However, the scaffold presented no evidence of fracture from the physical bench test, even when significantly over-expanded, as shown in **Fig.13** and so high levels of plastic strain may not pose a threat to the scaffold's structural integrity within reasonable limits.

In contrast, the best prediction of the *RS* is given by model 1-Cir-TrIso-Hill-Y which used the slower displacement rate stress-strain data, transverse isotropy as well as incorporating the failure data. This yielded a percentage error of 8.99% compared to the *in-vitro* test. The force-displacement curves for test model 1-Cir-TrIso-Hill-Y and the *in-vitro* test are given in **Fig.10**. Observation of **Fig.10** shows that material model 1-Cir-TrIso-Hill-Y captured the general force-displacement profile of the scaffold well although with a small over prediction in maximum force but a similar gradient

of the curve, representing the scaffold's stiffness.

Accurate prediction of both the post-expansion scaffold diameter and specific radial strength does not appear to be possible within the constraints of the constitutive theory in the in-built Abaqus/CAE anisotropic plastic potential models investigated. Therefore, a higher fidelity material model must be explored.

4.4 Hoddy-Bressloff Material Model

Based on the findings from the *in-silico* test scenarios 1 - 10 it was hypothesised that an alternative model may be able to achieve a more accurate estimation of the radial strength whilst minimising the compromise in prediction of the post-expansion scaffold shape.

Thus the Hoddy-Bressloff model was devised to:

1. More accurately model the high strain behaviour of the axial direction.
2. Capture the stress relaxation and subsequent decrease in hardening in elements that become overly strained.

This improved model facilitates greater plastic strains to develop in some elements as they become overly strained and exhibit a large drop in stress whilst retaining radial strength in the scaffold overall via the increase in yield stress and hardening in the axial direction as the plastic strain develops. Further, the stress-strain data at 1 mm/min was used to calibrate the model along with the implementation of isotropic elasticity theory.

The Hoddy-Bressloff model achieved a good level of accuracy in predicting the final shape of the scaffold post expansion, in particular for a model that utilises the stress-strain data obtained at the slower, more realistic displacement rate. Percentage errors for prediction of the FD of 5.46% and 5.39% for rings 1 and 6, respectively were achieved. The model also predicted the RS with an accuracy of 4.45% in test scenario 11 which represents the best estimation of this metric compared to all the aforementioned models. It should be noted that the elasto-plastic model utilised by Wang et al. (2018) in the expansion of a polymeric BRS achieves a similar level of percentage recoil. However, the scaffold width and thickness are far greater than that of the ArterioSorb^{TM} BRS. This is testament to the exceptional recoil behaviour of the ArterioSorb^{TM} which, as proven in this study, is extremely difficult to capture in tandem with an accurate RS prediction. Therefore, this model appears to offer a good balance of both scaffold shape and specific radial strength prediction. The model also estimates these critical metrics conservatively by under-predicting the radial strength

and over-predicting the scaffold elastic recoil which is favourable in contrast to over-estimating the performance of the device.

The distribution of PEEQ using model 1-Cir-Iso-HB-Y, scenario 11 at its post-expansion diameter is shown in **Fig.12**. This highlights that the model allowed significant plastic strain to develop at the inside of the crowns to a maximum value of almost 35. However, less than 1% of the elements in the scaffold display a value of $PEEQ$ greater than 1. The maximum values of PEEQ displayed in **Fig.11** would not manifest in *vitro* as fracture would occur prior to such high levels of $PEEQ$ developing. Again, it is interesting to note that the crowns joined to a connector display a much lower and more realistic distribution of PEEQ. This indicates that the crown geometry in the vicinity of a connector determines the mechanical performance of the scaffold. Otherwise RS may suffer considerably due to the significant levels of strain predicted at the inside of the crown. It is unclear to what extent scaffold struts of the ArterioSorb^{TM} BRS can withstand plastic strain before they fracture. Whilst tensile tests indicated a failure strain in the region of 0.8, *in-vitro* data suggested the scaffold can be greatly over-expanded without evidence of strut fracture, as shown in **Fig.13** and so it is highly likely the bending of the scaffold struts facilitates far greater strain to be tolerated. It is also noteworthy that the 'pinching' evident in the *in-vitro* test at the outside edge of the crown apex was also evident in model 1-Cir-Iso-HB-Y. Areas of modest but noticeable levels of plastic strain lie either side of the crown apex. However, the magnitude of PEEQ at the outside of the crown is certainly smaller than in the case of model 50-Cir-Iso-Hill-Y. Further, **Fig.11** appears to show the PEEQ is more confined to the vicinity of the crown and less well distributed into the scaffold struts in comparison to **Fig.8** and **Fig.9** which depict the in-built Abaqus/CAE anisotropic models.

Whilst model 1-Cir-Iso-HB-Y provides a reasonable prediction of the scaffold's final diameter, **Fig.15** shows that the scaffold recoiled more greatly *in-silico* than in the *in-vitro* test where the post-expansion recoil was extremely low.

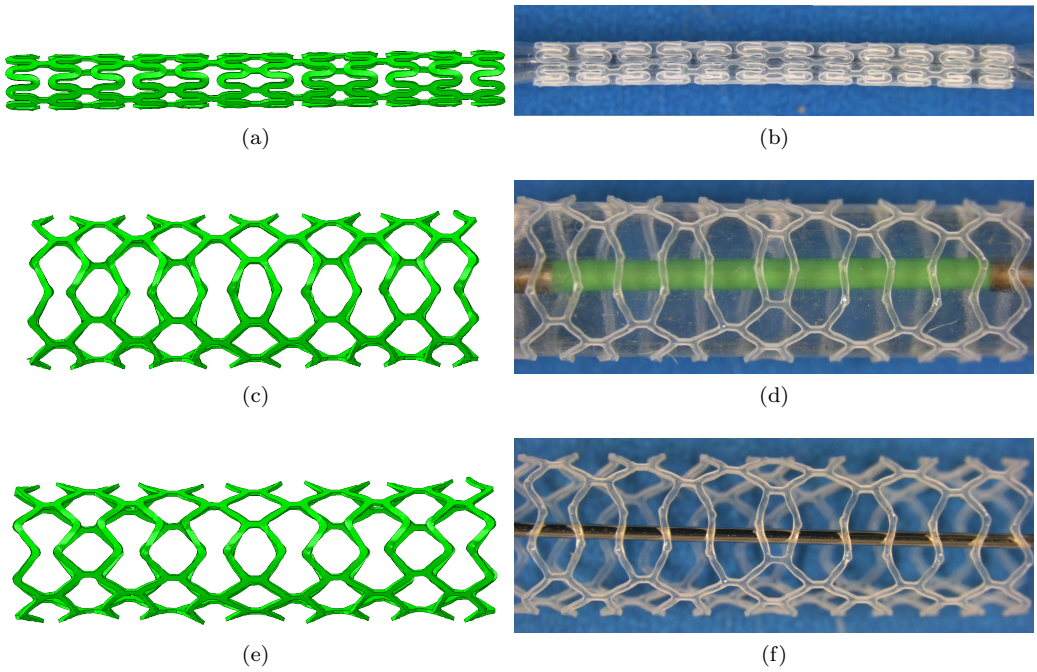

Figure 15: A comparison of the scaffold shapes for scenario 11 (left) and the in-vitro test (right). Scenario 11 utilises the Hoddy-Bressloff material model. Each stage of the deployment process is shown where **(a)** and **(b)** depict the scaffold post crimping, **(c)** and **(d)** depict the scaffold on the balloon at maximum inflation pressure and **(e)** and **(f)** depict the recoiled scaffold post expansion.

The maximum force required by the crimp to crush the scaffold is accurately predicted in model 1-Cir-Iso-HB-Y, as shown in **Fig.12**. Indeed, the slope of the curve which denotes the stiffness of the scaffold is also in agreement. However, as the scaffold begins to buckle and lose radial strength the curves diverge significantly. This is not a critical behaviour to model as the scaffold is already considered to have failed after the maximum force has been applied. The buckling of the scaffold is subject to many geometrical non-linearities that might initiate this, making it particularly hard (and unnecessary) to predict in this context.

4.5 Realistic Simulation Strategy

Whilst it was hypothesised that the disparity in recoil behaviour of the scaffold between the *in-silico* and *in-vitro* scenarios was, in part, due to the multiple balloon expansion strategy used in *vitro*, this was not found to be the case. Multiple balloon expansions of the scaffold is commonly used in clinical practice, known as pre/post dilation. The realistic simulation setup detailed in section 2.4

was utilised to explore whether this strategy yields improved recoil results, for the Hoddy-Bressloff model, detailed in **Table.3**, model 1-Cir-Iso-HB-Y*.

Model 1-Cir-Iso-HB-Y* yielded no significant improvement in prediction of the final scaffold shape with very similar levels of $R_{\%}$ and FD compared to scenario model 1-Cir-Iso-HB-Y. However, prediction of RS did improve and achieved a percentage error of just 1.1% compared to the *in-vitro* test. The force-displacement curve for this test case, shown in **Fig.12** displays good agreement with the *in-vitro* data until the point of maximum force, after which, again, the curves diverge significantly. The final diameter of the scaffold was predicted with percentage errors of 4.9% and 6.7% compared to the *in-vitro* test for rings 1 and 6, respectively. However, the higher complexity of these simulations means that solution times were in the order of 20 hours, rather than 6 hours, achieved by the single balloon strategy. Therefore, this strategy is difficult to justify given the practicalities of long solution times and the volume of the results files produced, particularly in the case of a design study where multiple simulations are required.

These findings confirm that a mechanism exists in the PLLA, that is not currently captured by any of the aforementioned models, which results in the low recoil behaviour of the ArterioSorb^{TM} BRS. Therefore, the exploration of alternative material models to capture this low recoil behaviour without alteration of the RS prediction, should be undertaken. The use of parallel network models to capture the viscoelasticity observed in PLLA should certainly be considered. However, whilst a number of previous studies develop and utilise such constitutive material models (Bobel et al. 2015, Bobel & McHugh 2018, Debusschere et al. 2015, Eswaran et al. 2011, Bergström & Boyce 2001), it is unclear whether they would facilitate accurately capturing the recoil behaviour of a thin-strut second generation BRS, particularly given the very low values exhibited in the ArterioSorb^{TM} BRS. No previous studies appear to report a $R_{\%}$ of less than 3% for a thin-strut BRS deployed via balloon expansion. It may be necessary to simulate the deployment of BRS in the natural time scale of the expansion method to fully realise the benefits of a viscoelastic model, especially given that the slow deformation of polymers increases the plastic flow that occurs, which will benefit the scaffold recoil (Bobel & McHugh 2018) albeit, in the haemodynamic environment, the efficacy of this phenomenon may be lessened as per the considerations of Wang et al. (2018). Whilst a viscoelastic model may reduce the recoil by effectively damping the response of the PLLA as it begins to recoil, it will not alter the final steady state response of the scaffold but result in a time dependant creep phenomenon occurring. It should also be noted that the *in-vitro* tests were not conducted to observe creep of the scaffold and so the actual recoil values could be slightly higher than recorded, leading to further

improved accuracy of the Hoddy-Bressloff model in capturing the final scaffold shape. The use of a viscoelastic model could also lead to an increase in solution times in the FEA simulations and require a more complex calibration process to fit the material data to the constitutive model.

Whilst the multi-balloon expansion technique has been modelled, a realistic multi-stage elevated temperature crimping process was not able to be explored in this work. It is possible that this process, conducted by Arterius Ltd, has a significant impact on the recoil behaviour of the scaffold due to the rearrangement of polymer chains that occurs throughout this process. Therefore, to explore this also could provide further insight in the the low recoil behaviour of the ArterioSorb^{TM} BRS.

5 Limitations and Future Work

- It is widely understood that the mechanical behaviour of PLLA displays significant temperature dependency. However, the stress-strain data from the uni-axial tensile tests was obtained at room temperature despite the *in-vitro* mechanical testing being conducted at an elevated temperature. This was due to the testing equipment available. Investigation of the effect of elevated temperature on the stress-strain behaviour could provide further insight into the modelling of PLLA and in particular the recoil behaviour of the ArterioSorb^{TM} BRS.

- If temperature dependant stress-strain data could be obtained then the *in-silico* crimping process could more closely match the *in-vitro* process which may help to improve prediction of the final scaffold shape and help to uncover the mechanism through which the ArterioSorb^{TM} achieves such low percentage recoil behaviour.

- Exploration of other material models beyond the simple elasto-plastic theory considered here should be undertaken. In particular, the viscoelasticity observed in PLLA should be explored via the use of parallel network models.

6 Conclusions

This work compares and contrasts a variety of material models, including a new user-defined model, calibrated with realistic stress-strain data obtained from uniaxial tensile tests and validates them with clinically relevant *in-vitro* data. An improved simulation strategy that offers closer alignment

with the *in-vitro* tests was also explored to attempt to further improve *in-silico* prediction of scaffold performance. From this, the following conclusions can be drawn.

1. A new material property model, the Hoddy-Bressloff model, provides an improved yet conservative estimation of radial strength with a percentage error of just 1.1% using a realistic multi-balloon expansion strategy. Post-expansion scaffold shape is predicted within 6.7% of the *in-vitro* data.

2. The realistic simulation setup indicates that a mechanism exists in the PLLA which causes the very low recoil behaviour of the ArterioSorb^{TM} BRS that is not captured in the aforementioned elasto-plastic material models. Therefore, higher fidelity, viscoelastic material models should be explored to attempt to describe this mechanism that reduces the recovered elastic strain as well as exploration of the effect of the crimping process of scaffold mechanical behaviour.

3. It appears the ArterioSorb^{TM} can withstand higher plastic strain than indicated in the uniaxial tensile tests. A mechanism exists in bending of the PLLA that facilitates greater tolerance of plastic strain before fracture is initiated.

4. Capturing both the post-expansion scaffold shape and specific radial strength in *silico* for the ArterioSorb^{TM} BRS cannot be achieved with the in-built Abaqus (DS SIMULIA) anisotropic models explored in this study.

5. An anisotropic description of the plastic behaviour of the scaffold is superior to an isotropic model to accurately capture the scaffold mechanical behaviour.

6. When using an anisotropic plastic potential model that incorporates the stress relaxation data along with isotropic elastic theory and stress-strain data obtained at a fast displacement rate of 50 mm/min, an improvement in accuracy for scaffold shape prediction can be achieved.

7. In contrast, when using an anisotropic plastic potential model that incorporates the stress relaxation data along with a transverse isotropy approximation, the model should utilise stress-strain data obtained at a slow, clinically relevant displacement rate, in this case 1 mm/min to more accurately capture the specific radial strength of the scaffold.

Acknowledgements

This work was funded by the engineering and physical sciences research council.

References

Abaqus 6.21 Analysis User's Manual (2018).

Abizaid, A., Kedev, S., Mohd Ali, R. B., Santoso, T., Cequier, A., van Geuns, R., Chevalier, B., Hellig, F., Costa, R. & Onuma, Y. (2019), 'Tct-176 implantation of thin-strut sirolimus-eluting bioresorbable vascular scaffold in patients with de novo coronary artery lesions: 2-year clinical and 6-month imaging outcomes of the meres-1 extend trial', *Journal of the American College of Cardiology* **74**(13S), B175–B175.

Al-Lamee, K. G., Kelly, A., Coates, P., Thompson, G. & Coton-Rose, P. (2019), *US 10,299,944 B2* .

Amadei, B. (1996), Importance of anisotropy when estimating and measuring in situ stresses in rock, *in* 'International Journal of Rock Mechanics and Mining Sciences & Geomechanics Abstracts', Vol. 33, Elsevier, pp. 293–325.

Benham, P. P., Crawford, R. J. & Armstrong, C. G. (1996), *Mechanics of engineering materials*, Pearson.

Bergström, J. & Boyce, M. (2001), 'Constitutive modeling of the time-dependent and cyclic loading of elastomers and application to soft biological tissues', *Mechanics of materials* **33**(9), 523–530.

Bergstroem, J. S. & Hayman, D. (2016), 'An overview of mechanical properties and material modeling of polylactide (pla) for medical applications', *Annals of biomedical engineering* **44**(2), 330–340.

Bink, N., Mohan, V. B. & Fakirov, S. (2019), 'Recent advances in plastic stents: a comprehensive review', *International Journal of Polymeric Materials and Polymeric Biomaterials* pp. 1–22.

Blair, R., Dunne, N., Lennon, A. & Menary, G. (2019*a*), 'Characterisation and constitutive modelling of biaxially stretched poly (l-lactic acid) sheet for application in coronary stents', *Journal of the mechanical behavior of biomedical materials* **97**, 346–354.

Blair, R., Dunne, N., Lennon, A. & Menary, G. (2019*b*), 'Multi-objective optimisation of material properties and strut geometry for poly (l-lactic acid) coronary stents using response surface methodology', *BioRxiv* p. 667915.

Bobel, A. C., Lohfeld, S., Shirazi, R. N. & McHugh, P. E. (2016), 'Experimental mechanical testing of poly (l-lactide)(plla) to facilitate pre-degradation characteristics for application in cardiovascular stenting', *Polymer Testing* **54**, 150–158.

Bobel, A. C. & McHugh, P. E. (2018), 'Computational analysis of the utilisation of the shape memory effect and balloon expansion in fully polymeric stent deployment', *Cardiovascular engineering and technology* **9**(1), 60–72.

Bobel, A., Petisco, S., Sarasua, J. R., Wang, W. & McHugh, P. (2015), 'Computational bench testing to evaluate the short-term mechanical performance of a polymeric stent', *Cardiovascular engineering and technology* **6**(4), 519–532.

Bressloff, N. W., Pant, S. & Al-Lamee, K. G. (2017), *US 9,707,109 B2* .

De Beule, M., Mortier, P., Carlier, S. G., Verhegghe, B., Van Impe, R. & Verdonck, P. (2008), 'Realistic finite element-based stent design: the impact of balloon folding', *Journal of Biomechanics* **41**(2), 383–389.

Debusschere, N., Segers, P., Dubruel, P., Verhegghe, B. & De Beule, M. (2015), 'A finite element strategy to investigate the free expansion behaviour of a biodegradable polymeric stent', *Journal of biomechanics* **48**(10), 2012–2018.

Eswaran, S. K., Kelley, J. A., Bergstrom, J. S. & Giddings, V. L. (2011), 'Material modeling of polylactide', *SIMULIA Customer Conference* pp. 1–11.

Etave, F., Finet, G., Boivin, M., Boyer, J.-C., Rioufol, G. & Thollet, G. (2001), 'Mechanical properties of coronary stents determined by using finite element analysis', *Journal of Biomechanics* **34**(8), 1065–1075.

Farah, S., Anderson, D. G. & Langer, R. (2016), 'Physical and mechanical properties of pla, and their functions in widespread applications—a comprehensive review', *Advanced drug delivery reviews* **107**, 367–392.

Grogan, J. A., Leen, S. B. & McHugh, P. E. (2012), 'Comparing coronary stent material performance on a common geometric platform through simulated bench testing', *Journal of the mechanical behavior of biomedical materials* **12**, 129–138.

Hill, R. (1948), 'A theory of the yielding and plastic flow of anisotropic metals', *Proceedings of the Royal Society of London. Series A. Mathematical and Physical Sciences* **193**(1033), 281–297.

Hoffmann, R., Mintz, G. S., Dussaillant, G. R., Popma, J. J., Pichard, A. D., Satler, L. F., Kent, K. M., Griffin, J. & Leon, M. B. (1996), 'Patterns and mechanisms of in-stent restenosis: a serial intravascular ultrasound study', *Circulation* **94**(6), 1247–1254.

Katagiri, Y., Torii, R., Takahashi, K., Tenekecioglu, E., Asano, T., Chichareon, P., Tomaniak, M., Piek, J. J., Wykrzykowska, J. J. & Bullett, N. (2019), 'Preclinical evaluation of a thin-strut bioresorbable scaffold (arteriosorb): acute-phase invasive imaging assessment and hemodynamic implication', *Eurointervention: Journal of Europcr in Collaboration with the Working Group on Interventional Cardiology of the European Society of Cardiology* .

Koltowski, L., Tomaniak, M., Ochijewicz, D., Maksym, J., Roleder, T., Zaleska, M., Proniewska, K., Opolski, G. & Kochman, J. (2020), 'Second generation, sirolimus-eluting, bioresorbable tyrocore scaffold implantation in patients with st-segment elevation myocardial infarction: Baseline oct and 30-day clinical outcomes–a fantom stemi pilot study', *Catheterization and Cardiovascular Interventions* **96**(1), E1–E7.

Lautrup, B. (2011), *Physics of continuous matter: exotic and everyday phenomena in the macroscopic world*, CRC press.

Nef, H., Wiebe, J., Boeder, N., Dörr, O., Bauer, T., Hauptmann, K., Latib, A., Colombo, A., Fischer, D. & Rudolph, T. (2018), 'A multicenter post-marketing evaluation of the elixir desolve® novolimus-eluting bioresorbable coronary scaffold system: First results from the desolve pmcf study', *Catheterization and Cardiovascular Interventions* **92**(6), 1021–1027.

Onuma, Y., Serruys, P. W., Gomez, J., de Bruyne, B., Dudek, D., Thuesen, L., Smits, P., Chevalier, B., McClean, D. & Koolen, J. (2011), 'Comparison of in vivo acute stent recoil between the bioresorbable everolimus-eluting coronary scaffolds (revision 1.0 and 1.1) and the metallic everolimus-eluting stent', *Catheterization and cardiovascular interventions* **78**(1), 3–12.

Pant, S., Bressloff, N. W. & Limbert, G. (2012), 'Geometry parameterization and multidisciplinary constrained optimization of coronary stents', *Biomechanics and modeling in mechanobiology* **11**(1-2), 61–82.

Pant, S., Limbert, G., Curzen, N. P. & Bressloff, N. W. (2011), 'Multiobjective design optimisation of coronary stents', *Biomaterials* **32**(31), 7755–73.

Pauck, R. & Reddy, B. (2015), 'Computational analysis of the radial mechanical performance of plla coronary artery stents', *Medical Engineering and Physics* **37**(1), 7–12.

Qiu, T., Song, M. & Zhao, L. (2017), 'A computational study of crimping and expansion of bioresorbable polymeric stents', *Mechanics of time-dependent materials* pp. 1–18.

Sadd, M. H. (2018), *Continuum Mechanics Modeling of Material Behavior*, Academic Press.

Vascular, A. (2017), 'Absorb bioresorbable vascular scaffold system information for prescribers'. **URL:** *https://vascular.eifu.abbott/en/hcp/home.html*

Wang, P.-J., Nezami, F. R., Gorji, M. B., Berti, F., Petrini, L., Wierzbicki, T., Migliavacca, F. & Edelman, E. R. (2018), 'Effect of working environment and procedural strategies on mechanical performance of bioresorbable vascular scaffolds', *Acta biomaterialia* **82**, 34–43.

Wang, Q., Fang, G., Zhao, Y., Wang, G. & Cai, T. (2017), 'Computational and experimental investigation into mechanical performances of poly-l-lactide acid (plla) coronary stents', *Journal of the mechanical behavior of biomedical materials* **65**, 415–427.